crystals

MDPI

Article

Abundant Catalytic Edge Sites in Few-Layer Horizontally Aligned MoS_2 Nanosheets Grown by Space-Confined Chemical Vapor Deposition

Alin Velea [1], Angel-Theodor Buruiana [1,2], Claudia Mihai [1], Elena Matei [1], Teddy Tite [1] and Florinel Sava [1,*]

[1] National Institute of Materials Physics, Atomistilor 405A, 077125 Magurele, Romania; alin.velea@infim.ro (A.V.); angel.buruiana@infim.ro (A.-T.B.); claudia.mihai@infim.ro (C.M.); elena.matei@infim.ro (E.M.); teddy.tite@infim.ro (T.T.)
[2] Faculty of Physics, University of Bucharest, Atomistilor 405, 077125 Magurele, Romania
* Correspondence: fsava@infim.ro

Abstract: Recently, a smart strategy for two-dimensional (2D) materials synthesis has emerged, namely space-confined chemical vapor deposition (CVD). Its extreme case is the microreactor method, in which the growth substrate is face-to-face stacked on the source substrate. In order to grow 2D transition metal dichalcogenides by this method, transition metal oxides, dispersed in very small amounts on the source substrate, are used as source materials in most of the published reports. In this paper, a colloidal dispersion of MoS_2 in saline solution is used and MoS_2 nanosheets with various shapes, sizes (between 5 and 60 μm) and thicknesses (2–4 layers) have been synthesized. Small MoS_2 flakes (regular or defective) are present on the surface of the nanosheets. Catalytic sites, undercoordinated atoms located at the edges of MoS_2 flakes and nanosheets, are produced in a high number by a layer-plus-island (Stranski–Krastanov) growth mechanism. Several double-resonance Raman bands (at 147, 177, 187, 225, 247, 375 cm^{-1}) are assignable to single phonon processes in which the excited electron is elastically scattered on a defect. The narrow 247 cm^{-1} peak is identified as a topological defect-activated peak. These findings highlight the potential of defect engineering in material property optimization, particularly for solar water splitting applications.

Keywords: 2D layered materials; transition metal dichalcogenide; space-confined chemical vapor deposition; microreactor; Raman spectroscopy

Citation: Velea, A.; Buruiana, A.-T.; Mihai, C.; Matei, E.; Tite, T.; Sava, F. Abundant Catalytic Edge Sites in Few-Layer Horizontally Aligned MoS_2 Nanosheets Grown by Space-Confined Chemical Vapor Deposition. *Crystals* **2024**, *14*, 551. https://doi.org/10.3390/cryst14060551

Academic Editor: Lin Gan

Received: 18 May 2024
Revised: 7 June 2024
Accepted: 12 June 2024
Published: 14 June 2024

1. Introduction

Quasi-two-dimensional (2D) crystalline semiconductor materials are anticipated to form the basis of next-generation high-performance nanoelectronics, optoelectronics, and photoelectrocatalysis. Transition metal dichalcogenides (TMDs) [1] are a prominent class of such 2D materials. The chemical formula of TMDs is MX_2, where M is a transition metal element from groups IVB (Ti, Zr or Hf), VB (V, Nb or Ta), VIB (Mo, W), VIIB (Re), or VIIIB (Pd, Pt), while X is a chalcogen element (S, Se, or Te) [2]. These 2D TMDs are crystalline molecular layers (monolayers), thicker than an atom and without dangling bonds, being the building blocks of the corresponding 3D crystals [3]. Each single crystalline MX_2 monolayer is a stack of three hexagonal monoelemental planes (X, M, X) bonded together by strong covalent bonds [–X–M–X–] [1,3], while the interactions between monolayers are of the van der Waals type [3].

Since 2004, researchers have been working to develop cost-effective, large-area fabrication techniques for producing 2D semiconductors with high crystallinity and excellent semiconducting properties [4]. Among these methods, vapor deposition, a bottom-up approach, is the most promising. Recently, a new vapor deposition strategy has emerged. It uses a microreactor and represents the extreme case of the method named space-confined vapor deposition [5,6]. In this technique, a confined environment is created by aligning

two substrates in a horizontal, face-to-face configuration. The "source substrate", typically positioned at the bottom, contains the source material, while the "growth substrate", placed on top, is left blank to allow for material deposition. The microreactor is heated in an inert atmosphere, inside of a quartz tube, using a tube furnace. The method's main advantage is the minimal amount of source materials required, which results in economic benefits. Moreover, the reduced nucleation density might facilitate the formation of large, high-quality 2D crystals.

Using variable parameters of this method, the type of transition metals source and the seeding method of the source substrate, crystalline 2D TMDs were obtained. Almost all published reports used a transition metal oxide precursor as the transition metals source. In these cases, the microreactor method is a variant of the chemical vapor deposition (CVD) method. The chalcogen source is positioned outside the microreactor, in the upstream heating zone of the furnace. The methods used for seeding the source substrate were drop casting of the colloidal dispersion [7,8], sputtering [7], spin coating of metal salts (such as Na_2WO_4 and Na_2MoO_4) [9], oxide powders spreading [10], and electron beam evaporation [11–13]. High quality results have also been achieved when the oxide source is outside the microreactor [14–16].

There is only one report that uses the TMD as a transition metal source, which was deposited onto source substrate by pulsed laser deposition (PLD) at room temperature [17].

Lateral (WS_2/MoS_2 [9]) and vertical (MoS_2/WSe_2 [18]) heterostructures have been also produced by the confined-space method.

In this study, we sought to produce crystalline 2D MoS_2 flakes using the space-confined vapor deposition method. We started with MoS_2 nanoparticles deposition on the source substrate by drop casting the colloidal dispersion of MoS_2. While there have been reports of large crystalline monolayer MoS_2 domains produced by physical MoS_2 vapor transport [19–22], our experiments showed that the MoS_2 nanoparticles did not sublimate up to a temperature of 1050 °C. Because some salts (e.g., NaCl) can dramatically decrease the melting point of metal oxide precursors [2], NaCl was added in the colloidal dispersion of MoS_2, and thus, we obtained 2D MoS_2 flakes at 980 °C. This paper investigates their properties.

2. Materials and Methods

The source of transition metal used in this study was MoS_2 powder (99.0% purity) with a particle size of less than 2 μm, purchased from Aldrich (Darmstadt, Germany). The key ingredient, NaCl (99.5% purity), was acquired from Fluka (Gillingham, UK). The deionized (DI) water used for colloidal dispersion was produced using a Barnstead Smart2Pure 3 UV Water Purification System from Thermo Scientific (Waltham, MA, USA).

Firstly, a colloidal dispersion of MoS_2 was prepared. A mixture of 57.7 mg of MoS_2 powder and 14.1 mg of NaCl were added to 15.8 mL of deionized water. This mixture was subjected to ultrasonication for 40 min, after which the obtained black suspension was left undisturbed for 24 h to allow particles to settle. Following this period, all heavy particles had settled at the bottom of the container, resulting in a transparent, clear MoS_2 colloidal dispersion (Figure 1). An ultra-thin gray film of hydrophobic MoS_2 particles was observed floating on the liquid surface, likely comprising non-monolayer nanometric particles [23].

The two substrates used were SiO_2 (300 nm)/Si pieces, each with a size of 1×1 cm^2. These were cleaned with acetone, isopropyl alcohol (IPA), and DI water. Two drops (2×0.2 mL) of the clear MoS_2 colloidal dispersion in the saline solution were spread onto the source substrate using a graduated pipette (Figure 1). This substrate was then vacuum-dried to expedite water evaporation. Following this, the growth substrate was placed over the source substrate, creating the confined space of a microreactor (Figure 1).

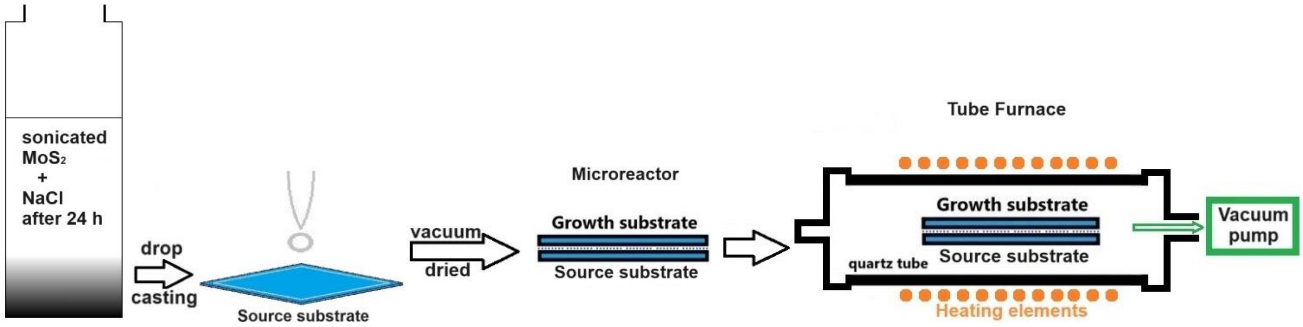

Figure 1. Schematic diagram of the process for the loading and preparation of the microreactor (sandwich-structured) configuration to produce MoS_2 nanosheets in a CVD furnace using the microreactor method (the extreme case of the space-confined chemical vapor deposition method).

The synthesis of 2D MoS_2 was carried out in a tube furnace setup (model CY-1200X-III-50IC from Zhengzhou CY Scientific Instrument, Zhengzhou, China), equipped with a 2" quartz tube, three controlled heating zones and a gas mixing system. The microreactor was placed horizontally in the quartz tube, which was sealed at both ends with flanges, and positioned in the center of one of heated zones (Figure 1). The oxygen was evacuated from the quartz tube through three vacuum/purging cycles using nitrogen (99.999% purity). Then, the quartz tube was evacuated to a pressure of 1.3 Pa, which was maintained until the samples' removal. The furnace was heated to 980 °C in 38 min, maintained at this temperature for 30 min, and then allowed to cool naturally to room temperature before the samples were extracted for investigation.

Optical microscopy images were captured using an OPTIKA (Budapest, Hungary) 50×–800× microscope, equipped with a trinocular, halogen light, and a polarizing kit.

Thickness measurements and atomic force microscopy (AFM) images were obtained utilizing an NT-MDT Aura Ntegra Prima (Amsterdam, The Netherlands) atomic force microscope in non-contact mode.

For morphological and elemental characterization, a Zeiss Gemini 500 scanning electron microscope (SEM) provided with an energy dispersive X-ray (EDX) spectrometer from Bruker (Billerica, MA, USA), was employed.

The micro-Raman spectra were recorded in the backscattering geometry using a LabRAM HR Evolution Raman spectrometer from HORIBA Jobin–Yvon (Palaiseau, France). The spectrometer was equipped with a confocal microscope and an He–Ne laser operating at an excitation wavelength of 633 nm. The laser radiation was focused onto the samples surface using an Olympus 100× objective (Tokyo, Japan). To avoid heating effects, the laser power was maintained at a suitable low level. The Raman shift was calibrated using the Si peak at 520 cm^{-1}.

3. Results

3.1. Optical and Atomic Force Microscopy

Figure 2a depicts the optical microscopy image of typical MoS_2 nanosheets grown via space-confined chemical vapor deposition. The as-grown MoS_2 nanosheets, which exhibit various shapes, including equilateral triangles, span sizes from 5 to 60 μm.

According to the AFM images, their surface is abundantly decorated with small, irregular flakes, approximately 0.9 μm in size, as can be seen in Figure 2b. Figure 2c shows that some of these flakes are monolayers with a thickness of ~0.8 nm [24], which have grown on top of the nanosheets. The nanosheets exhibit a thickness ranging between two and four layers. For instance, the one depicted in Figure 2b has a thickness of ~2.65 nm, which corresponds roughly to three layers.

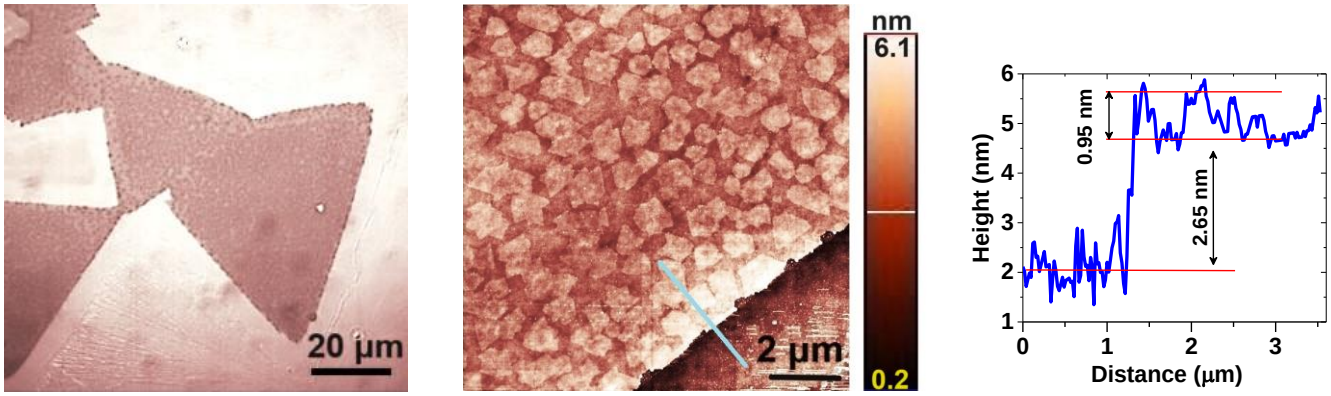

Figure 2. Representative (**a**) optical microscopy and (**b**) AFM images of large MoS_2 nanosheets; (**c**) the height profile obtained from the region indicated by the blue line in (**b**).

3.2. SEM and EDX

The SEM image depicted in Figure 3a shows one of the nanosheets with sharp edges, proving the crystalline nature of the MoS_2 nanosheets.

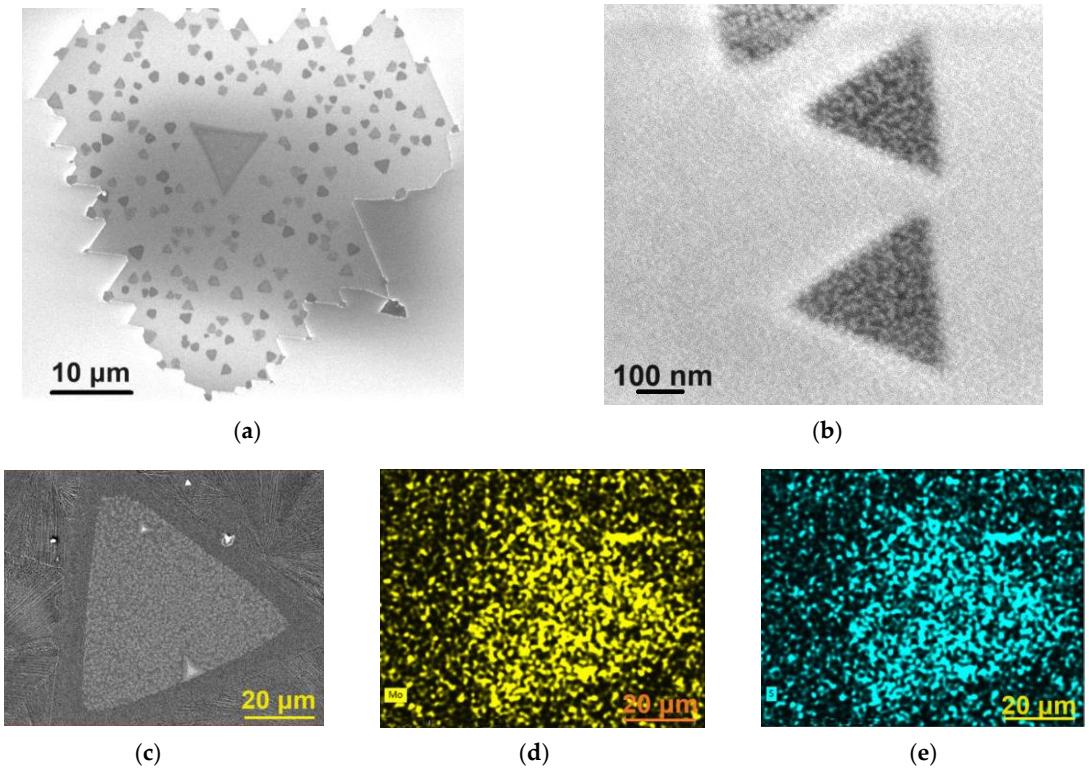

Figure 3. SEM images of (**a**) MoS_2 nanosheet and (**b**) MoS_2 flakes grown on the surface of the MoS_2 nanosheet. SEM image of (**c**) MoS_2 nanosheet used in EDX mapping of (**d**) molybdenum and (**e**) sulfur.

When the MoS_2 flakes, grown on top of the MoS_2 nanosheets, are sparse, as seen in Figure 3a, they exhibit more regular shapes, often equilateral triangles, as shown in Figure 3b. These additional flakes become more irregular (Figure 2b) when the number of these flakes increases and the space between them decreases. Many of them are monolayers or bilayers (multilayer flakes are exceptions, as the Raman spectra will prove).

The analysis of the EDX spectra revealed that, within the limits of experimental errors, the nanosheets exhibited a sulfur deficiency in their composition, an observation

consistent with MoS_2 nanosheets prepared by other bottom-up methods [25,26]. For example, the nanosheet shown in the Figure 2b has an average composition of $MoS_{1.33}$. Furthermore, within the limits of experimental errors, no traces of Cl or Na were detected in the nanosheets. Figure 3c shows the SEM image of a MoS_2 nanosheet used in EDX mapping, while Figure 3d,e present the corresponding EDX maps of molybdenum and sulfur, respectively.

3.3. Raman Spectroscopy

The micro-Raman spectra were recorded in the range 100÷530 cm^{-1}, using a 632.8 nm excitation line across different MoS_2 nanosheets in an ambient air environment. Figure 4a depicts the spectra for several microzones (a1, a2, a3, and b) on two distinct nanosheets, see Figure 4b,c. The morphology of the microzone (a3) is typical for most nanosheets, while that of the microzones (a1), (a2), and (b) are exceptions.

The intensity of the spectra decreases from (a1) to (b) relative to the silicon peak, indicating a decrease in the average thickness of the microzones. There are more Raman peaks than the two zone-center first-order Raman active modes, $E^1_{2g}(\Gamma)$ and $A_{1g}(\Gamma)$, expected for hexagonal *2H*-MoS_2, bulk or nanosheets with at least 5 layers, at 382 cm^{-1} and 407 cm^{-1}, respectively, in backscattering geometry and without monochromators [27–29].

The $A_{1g}(\Gamma)$ peak frequency is thickness-dependent, red-shifted as the number of layers decreases below 5, while $E^1_{2g}(\Gamma)$ is less blue-shifted [27]. For such thinner MoS_2 nanosheets, the frequency difference (δ) of the two Raman modes, with values of 19, 21, 22, 23, and 25 cm^{-1}, serves as an indicator of the number (n_m) of MoS_2 layers (n_m is 1, 2, 3, 4, and ≥5, respectively) [27]. However, this correlation, $n_m = f(\delta)$, may become inaccurate in nanosheets presenting strain, doping, defects, and ionic substitution or adsorption [30].

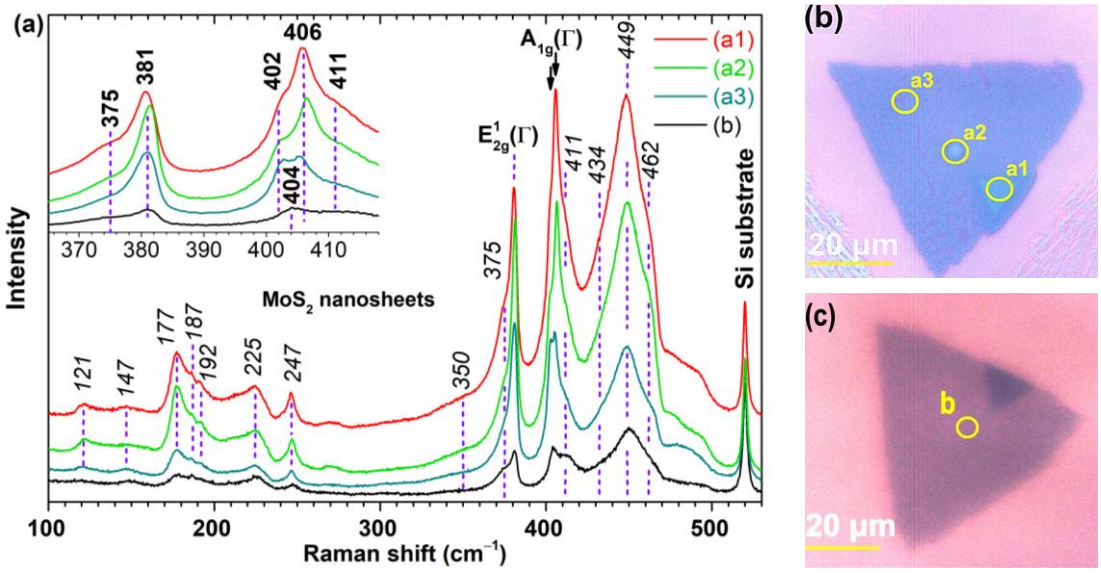

Figure 4. Raman scattering of MoS_2 nanosheets. (**a**) Raman spectra of selected microzones (a1, a2, a3, and b) on two MoS_2 nanosheets. All spectra are normalized relative to the Raman peak of the silicon substrate and have been vertically offset for enhanced visual clarity. (**b**,**c**) The corresponding optical images of the nanosheets.

The spectrum (a1) in Figure 4a exhibits δ as 25 cm^{-1} (likely representing 5 layers) but it also has a shoulder at 402 cm^{-1} (δ = 21 cm^{-1}), corresponding to 2 layers. The intensity of the $A_{1g}(\Gamma)$ peak at 406 cm^{-1} surpasses that of $E^1_{2g}(\Gamma)$, an aspect also observed in thick nanosheets obtained by mechanical exfoliation under the resonance condition [27]. Therefore, it can be inferred that submicron holes exist within that thicker region of the nanosheet. A similar δ value was found for spectrum (a2), but the intensities of the two Raman modes, $E^1_{2g}(\Gamma)$ and $A_{1g}(\Gamma)$, are almost equal, indicative of a small number of layers

(up to 4) [27]. Due to the overall lower intensity of the spectrum (a2) compared to (a1), it is possible that the (a2) microzone consists of four layers, with sparse holes of two layers. The spectrum of the (a3) microzone on the same nanosheet, shows that the two $A_{1g}(\Gamma)$ peaks at 403 and 405 cm^{-1}, have the same intensity, suggesting a similar proportion of holes (2 layers) and plateaus (4 layers). The spectrum (b) exhibits a single $A_{1g}(\Gamma)$ peak at 404 cm^{-1} and, considering its smallest overall intensity, it is suggested that the microzone (b) mainly consists of 3 layers (δ = 23 cm^{-1}). All these assumptions are validated by the details observed in the regions highlighted on the optical images in Figure 4b,c, but also in Figure 2c.

In order to assign vibrational modes to the other Raman peaks, we rely on findings of other research groups. They propose that these peaks result from two primary factors: double resonant Raman scattering and the presence of defects in MoS_2 crystallites.

Let us first discuss how double resonant Raman scattering occurs. The calculated indirect band gap for bulk MoS_2 is 1.23 eV [31] and it goes from Γ point to ~Q point in the Brillouin zone [32]. As the number of layers in MoS_2 flakes decreases below 4 [33], the bandgap begins to widen up to 1.87–1.92 eV [31] (these are experimentally obtained direct band gaps at the K point of the Brillouin zone for MoS_2 monolayers). When laser energy (1.96 eV for 632.8 nm in our case) has values close to the absorption edge of bulk MoS_2, between 1.833 and 2.410 eV (676.4 to 514.5 nm), both the indirect and direct band gaps are strongly and mediumly, respectively, modulated by A_{1g} mode displacements. Thus, periodically over time, bulk MoS_2 becomes a material with a direct band gap and the excitation laser line resonates with the vertical electronic transitions in the K point [29]. In other words, there is a strong coupling between the electronic band structure and some lattice vibrational modes (the $E^1{}_{2g}$ mode couples only very weakly to the electronic structure [29]). As a result, the A_{1g} peak is enhanced in relation to the $E^1{}_{2g}$ peak [27]. Such an enhancement disappears for ultrathin MoS_2 nanosheets [27], as can also be seen in Figure 4a, indicating that the coupling between electronic transition at the K point with the A_{1g} mode is weaker than in bulk.

However, not all TMDs exhibit additional Raman peaks [34] despite the laser energies being close to the absorption edges (first resonance: the optical excitation energy matches a vertical electronic transition). An additional requirement is the existence of excitons in the TMDs optical absorption spectrum, which are strongly coupled with specific phonon modes and resonate (the second resonance) with the electronic band structure. In MoS_2, these excitons at 1.88 eV and 2.06 eV for bulk [29] and 1.85 and 1.97 eV for monolayer [27] are linked to the transitions at the K point of the Brillouin zone, between spin-orbit split states in valence band and a degenerate state in the conduction band [32]. Thus, double resonant Raman (DRR) scattering processes enhance the second-order (or multiphonon) Raman scattering modes [34–36].

For a wide range of materials, including TMDs [34], the observed multiphonon scattering peaks in Raman spectroscopy can generally be categorized into two types [36]:

1. Overtone (for instance 2×), combination (sum) or difference bands of the phonons with zero momentum (at the Γ point of the Brillouin zone);
2. Overtone, combination or difference bands of phonons with nonzero momentum (for example, at the M point of the Brillouin zone [35]).

Experimental data reveal that variation in the excitation energy within the A and B excitonic level range yield different DRR spectra [36–38]. Consequently, DRR processes select other electronic states, in the K and Q valleys, and pairs of phonons, which have opposite momenta in the case of overtone (2×). They can be located either within the interior or at the edge of the Brillouin zone [37,38]. However, some restrictions exist: at the M point, the phonon combinations with different inversion symmetry (g or u) are not allowed [36]. Another interesting aspect of the DRR process is that even if certain first-order phonons are not observed in the Raman spectrum, they can participate in the formation of multiphonon bands [37]. Also, it is worth noting that the intensities of these multiphonon bands vary with temperature.

Hexagonal *2H*-MoS_2 presents 18 branches of the phonon dispersion relation [36]. In the center of the Brillouin zone (Γ), their symmetries are as follows:

1. E^2_{2g} (degenerate), E_{1g} (degenerate), E^1_{2g} (degenerate), and A_{1g}—four Raman-active modes;
2. E^1_{1u} (degenerate) and A^1_{2u}—two IR-active modes;
3. B^2_{2g}, E_{2u} (degenerate), B_{1u}, and B^1_{2g}—four silent modes;
4. E^2_{1u} (degenerate) and A^2_{2u}—two acoustic modes.

At the M point of the Brillouin zone, all phonons (called zone-edge phonons) are non-degenerate [36]. For instance, the doubly degenerate Γ-point phonon with E_{1g} symmetry, extends and splits into two distinct phonons, E_{1g} (M_1) and E_{1g} (M_2), at the M point. Here, there are also acoustic phonons (longitudinal LA, transverse TA, or out-of-plane transverse ZA) and quasi-acoustic optical phonons (LA′, TA′, or ZA′) [36].

At the K point, there are only two doubly degenerate phonons, $E_{ug}(K_1)$ and $E_{ug}(K_2)$, which originate from $E_{1g}(M_1)$, $E_{2u}(M_2)$, and $E^1_{2g}(M_1)$, $E^1_{1u}(M_2)$, respectively [36].

We have managed to assign all experimental Raman peaks in the (a1)–(a3), and (b) spectra, see Figure 4a and Table 1, using the frequencies of some first-order phonons in hexagonal *2H*-MoS_2 [36], as well as frequencies of second-order modes calculated based on the first-order phonon frequencies [36]. The frequencies of first-order phonons at Γ point were experimentally measured at 300 K [36]. The frequencies of first-order phonons at the M and K points, theoretically calculated at 0 K [36], were reduced by 2 cm^{-1} [36] to obtain their room temperature counterparts.

Table 1. The experimental Raman shifts ($\Delta\tilde{\upsilon}_{exp}$) along with their corresponding symmetry assignments, as reported in previous studies [35–37], for the bands observed in the resonance Raman spectra of *2H*-MoS_2 nanosheets. The measurements were conducted at room temperature, in an air ambient environment, using the incident light wavelength of 632.8 nm. A van Hove singularity between K and M is denoted by "vHs".

$\Delta\tilde{\upsilon}_{exp}$ (cm^{-1})	Symmetry Assignment [36]						
	(cm^{-1})	1st Order			2nd Order		
		Γ	M	K	Γ	M	K
	35 32 [35]	$E^2_{2g}(\Gamma)$					
	58	$B^2_{2g}(\Gamma)$					
121	123 125					$A_{1g}(\Gamma) - E_{1g}(\Gamma)$ $E^1_{1u}(M_2) - E^2_{1u}(M_1)$ $E^1_{2g}(M_1) - E^2_{1u}(M_1)$	
147	145						$E_{ug}(K_1) - A^2_{2u}(K)$
	146				$E^2_{2g}(M_1) - E_{1g}(M_1)$		$E_{ug}(K_1) - B^2_{2g}(K)$ $B^1_{2g}(K) - E^2_{1u}(K_2)$
	148						$E^1_{2g}(K_2) - E^2_{2g}(K_2)$ $E_{2u}(K_1) - E^2_{1u}(K_1)$
	154 158		$E^2_{1u}(M_2) = TA(M)$ $E^2_{2g}(M_1) = TA'(M)$				
177	175 176 179		$B^2_{2g}(M) = ZA'(M)$			$B_{1u}(M) - E^2_{1u}(M_1)$ $A_{1g}(M) - E^2_{2g}(M_2)$	
	182 183			$B^2_{2g}(K) = ZA'(K)$ $A^2_{2u}(K) = ZA(K)$			

Table 1. *Cont.*

$\Delta\tilde{\upsilon}_{exp}$ (cm^{-1})	(cm^{-1})	Symmetry Assignment [36]					
		1st Order			2nd Order		
		Γ	M	K	Γ	M	K
187	188			$E^2{}_{1u}(K_1)$ = TA(K)			
192	193					$E^1{}_{2g}(M_2) - B^2{}_{2g}(M)$	
225	228				$E_{1g}(\Gamma) - B^2{}_{2g}(\Gamma)$		
	227			vHs^1			
				vHs^2			
	231		$E^2{}_{2g}(M_2)$ = LA′(M)				
	232		$E^2{}_{1u}(K_2)$ = LA(K)				
	233		$E^2{}_{1u}(M_1)$ = LA(M)				
	235		$E^2{}_{2g}(K_2)$ = LA′(K)				
247	252					$A_{1g}(M) - E^2{}_{2g}(M_1)$	
	286	$E_{1g}(\Gamma)$					
	304		$E_{1g}(M_1)$				
	328			$E_{ug}(K_1)$			
	336			$E_{2u}(K_1)$			
350	350					$2 \times B^2{}_{2g}(M)$	
	368		$E^1{}_{2g}(M_2)$				
	374					$A_{1g}(\Gamma) - E^2{}_{2g}(\Gamma)$	
375	378			$B^1{}_{2g}(K)$ $A^1{}_{2u}(K)$			
381	383	$E^1{}_{2g}(\Gamma)$		$E^1{}_{2g}(K_2)$			
406	403	$B_{1u}(\Gamma)$					
	409	$A_{1g}(\Gamma)$	$B_{1u}(M)$				
411	410		$A_{1g}(M)$				
434	440					$B^1{}_{2g}(\Gamma) - E^2{}_{2g}(\Gamma)$	
	441					$E^1{}_{2g}(\Gamma) + B^2{}_{2g}(\Gamma)$	
449	453 455 [37]				combination between the van Hove singularities of two branches, vHs^1 and vHs^2, that fall at about the same frequency		
462	462					$E^2{}_{2g}(M_1) + E_{1g}(M_1)$ $2 \times E^2{}_{2g}(M_2)$	
	464					$E^2{}_{2g}(M_2) + E^2{}_{1u}(M_1)$	$2 \times E^2{}_{1u}(K_2)$

As can be seen in Table 1, most double resonant second-order Raman processes predominantly involve M-point phonons; those between K-point phonons are less common. This aligns with the widely accepted viewpoint that these bands originate from phonons with a wavevector $\mathbf{q} > 0$. Interestingly, we note that in Table 1, some frequencies of the resonant second-order Raman processes occurring between Γ-point phonons ($\mathbf{q} \cong 0$) align closely with the experimental values, mirroring observations in Ref. [36].

While the assignment of Raman bands is potentially error prone due to the accuracy of theoretical calculations, the Raman experiments carried out across different states of the same sample provide more reliable insights. Some studies indicate that the quality of the MoS_2 nanosheets can be inferred from the DRR spectra. For instance, it has been demonstrated [37,39] that defects (such as vacancies, anti-site defects) and strain (whether tensile or compressive), which arise in high quality MoS_2 monolayers obtained by mechanical exfoliation of a *2H*-MoS_2 crystal, trigger the emergence of the Raman bands (termed "defect-activated peaks") in the frequencies range below $E^1{}_{2g}(\Gamma)$. In the absence of such defects, this spectrum region has no Raman peaks, such as in case of the pristine samples. Furthermore, the intensity of defect-activated peaks is inversely proportional to $L^2{}_D$ (where L_D denotes the average inter-defect distance [39]). These observations likely hold true for nanosheets with thickness of a few layers.

We can find similarities in the positions of the defect-activated peaks for monolayers with L_D ~ 2.2 nm [39] with those in our Raman spectra, barring the difference in intensity and full width at half maxima. In the defective monolayers, the DRR process involves a single phonon, the momentum conservation being achieved by elastic scattering of the excited electron on a defect [39]. Our nanosheets exhibit a few Raman peaks (at 147, 177, 187, 225, 247, and 375 cm^{-1}) to which a single phonon can be assigned. However, as indicated in Table 1, two-phonon assignment is also possible. Additionally, certain Raman peaks (at 121 and 350 cm^{-1}) can be exclusively explained by a two-phonon assignment. While these findings add complexity to the process of quantifying the crystallinity of the MoS_2 nanosheets, they also distinctly point to the presence of defects within their structure.

An intriguing peak is the narrow one from 247 cm^{-1}, exhibiting an intensity (I_{247}) comparable to that of the peak at 225 cm^{-1} (I_{vHs}). The ratios $I_{2\times vHs}/I_{247}$ in the (a1)–(a3) and (b) spectra are 8.2, 7.4, 7.7, and 10.2, respectively. To the best of our knowledge, only one study reports this peak in Raman spectra of the MoS_2 fullerene-like structures [29], where its intensity is considerably lower. Thus, this peak likely emerges due to a substantially higher concentration of topological defects in nanosheets compared to MoS_2 fullerene-like structures. Such topological defects are identified as Stone–Wales type [40]. Such a defect appears through the topological transformation of four adjacent six-membered rings (each composed of three Mo and three S atoms) into two five-membered rings (FmR) and two seven-membered rings (SmR). One of the two FmR is composed of three Mo and two S atoms, and the other one is consisting of two Mo and three S atoms. One SmR includes an extra sulfur atom and the other SmR includes an additional Mo atom. In fullerene-like structures, the topological defects are five-membered rings, each of them being surrounded by five six-membered rings [41]. In Table 1, for the 247 cm^{-1} peak, a single phonon assignment could be $E^2{}_{2g}(K_2)$ = LA′(K) (at 235 cm^{-1}), while a two-phonon assignment, $A_{1g}(M) - E^2{}_{2g}(M_1)$ at 252 cm^{-1}, presents a closer match. Despite this, we propose that the single phonon assignment is more likely. Consequently, microzone (b) appears to have the lowest concentration of topological defects.

Another focal point for discussion is the Raman band (2 × vHs) at 449 cm^{-1}, which is a combination between the van Hove singularities (vHs) of two branches, between K and M, that fall around the same frequency (225 cm^{-1}) [36]. According to other reports [37,39], its intensity ($I_{2\times vHs}$) decreases with increasing defect concentration in the MoS_2 monolayer, whereas the intensity of the first-order peak (I_{vHs}) increases. In spectra (a1)–(a3), and (b) in Figure 4a, the ratios $I_{2\times vHs}/I_{vHs}$ decrease as 9, 8.4, 7.3, and 4.6, respectively. This implies an increase in defect concentration (other than topological defects), peaking in zone (b).

4. Discussion

Two-dimensional crystalline materials, being inherently anisotropic, can grow, in relation to the substrate, with molecular layers aligned in two complementary directions: horizontal and vertical [42].

For applications in nanoelectronics [43] and optoelectronics [44], the horizontal orientation of molecular layers is often preferred due to the need for high crystallinity (very low defect density) and large surface areas. However, this configuration tends to make the surface of these 2D materials catalytically inactive, as only the sulfur atoms along their edges exhibit significant catalytic activity [45]. Therefore, maximizing the number of active sites is crucial for catalytic applications. Strategies such as creating large quantities of small nanosheets or engineering defective surfaces are considered [45–48].

In the case of the vertical morphology, the active edge sites are naturally and abundantly present at the edges of the MoS_2 layers [42]. Kumara et al. [49] successfully grew vertically aligned MoS_2 flakes on top of horizontally aligned monolayer/bilayer MoS_2 sheets using conventional CVD methods.

These approaches demonstrate how different growth orientations of 2D materials can be strategically employed to enhance specific properties which are important in various technological applications.

In this study, using space-confined chemical vapor deposition, the objective to maximize the number of active edge sites in horizontally aligned *2H*-MoS_2 nanosheets is achieved due to the abundant presence on their surface of smaller, horizontally aligned MoS_2 flakes. Undoubtedly, various point defect species [26], also catalytically active [50], are present in different concentrations within the surface of both MoS_2 nanosheets and flakes, as Raman spectroscopy revealed. The edge sites are abundantly present in our samples and their catalytic activity has been proven [51,52].

The nanosheets consist of the *2H*-MoS_2 phase (according to the Raman spectra). The *1T*-MoS_2 phase appears to be absent, indicated by the lack of its characteristic peaks at 156 and 333 cm^{-1} [53]. The growth mechanism follows a layer-plus-island (Stranski–Krastanov) model: an initial multilayer structure comprising of two to three layers forms, on top of which additional flakes grow, varying in abundance and regularity. Two factors influence this growth process as follows: (i) the presence of chlorine vapors which react with the MoS_x groups ($x < 2$) at the edges of the MoS_2 source nanoparticles to form MoS_yCl_z ($0 < y \leq x < 2$) vapors. These vapors condense on the growth substrate, forming small nuclei with high mobility which continually attach to the edges of the growing MoS_2 nanosheets [2]. The chlorine is then removed through a self-purification process; and (ii) the extremely low amount of source materials, specific to the microreactor method, causes a significant decrease in the MoS_yCl_z vapor pressure towards the end of the deposition time. This reduction in vapor pressure leads to the decrease in the growth rate, resulting in the formation of MoS_2 flakes on top of the previously formed nanosheets.

The entire surface of the substrate (or electrode) can be completely coated with a few-layer horizontally aligned MoS_2 nanosheets decorated with MoS_2 flakes, through the appropriate increase of the deposition parameters (deposition time and amount of source materials).

5. Conclusions

We report a route that uses a microreactor, the extreme case of space-confined chemical vapor deposition, that can coat a substrate (or an electrode) with few-layer horizontally aligned *2H*-MoS_2 nanosheets, decorated with a varying amount of regular or defective MoS_2 flakes. This method significantly increases the concentration of catalytically active edge sites; more precisely, the undercoordinated atoms located at the edges of the MoS_2 flakes. The growth mechanism follows the layer-plus-island (Stranski–Krastanov) model, as revealed by optical, AFM, and SEM images. EDX and double-resonance Raman (DRR) spectra indicate the presence of defects (vacancies, anti-site defects, and topological defects) and strain (tensile or compressive) in varying concentrations across all nanosheets and flakes, in addition to the undercoordinated edge atoms. Resonant second-order Raman processes predominantly involve M-point phonons, but K-point or Γ-point phonons also align well with the experimental values. DRR bands at 147, 177, 187, 225, 247, and 375 cm^{-1} can be assigned to a single phonon process facilitated by elastic scattering of excited electrons on defects, though two-phonon assignments are also feasible. Raman peaks at 121 and 350 cm^{-1} can only be explained by two-phonon assignments. The narrow peak at 247 cm^{-1} is postulated to be a topological defect-activated peak, which is a rare finding in the literature. These results are significant to develop efficient photocatalysts (photoanode) made by low-cost, environmentally friendly, stable materials, for hydrogen production by water splitting using only sunlight as an energy source.

6. Patents

Florinel Sava, Alin Velea, Angel Theodor Buruiana, Claudia Mihai, Elena Matei, Teddy Tite have patent pending to State Office for Inventions and Trademarks—Romania, resulting from the work reported in this manuscript.

Author Contributions: Conceptualization, F.S.; methodology, F.S. and A.V.; validation, F.S.; formal analysis, F.S.; investigation, A.-T.B., E.M., T.T. and F.S.; resources, A.V.; writing—original draft preparation, F.S., A.V. and C.M.; writing—review and editing, F.S., A.V. and C.M.; visualization, F.S.;

project administration, A.V.; funding acquisition, F.S. and A.V. All authors have read and agreed to the published version of the manuscript.

Funding: This research was funded by the Core Program of the National Institute of Materials Physics, granted by the Romanian Ministry of Research, Innovation and Digitization through the Project PC3-PN23080303 and contract no. 21N/2019, additional act 11/2022. The authors kindly acknowledge the financial support of the Executive Unit for the Financing of Higher Education, Research, Development and Innovation (UEFISCDI) in the framework of the M-ERA.NET 109/2019 (ERANET-M.-2D-SPIN-MEM).

Data Availability Statement: All data generated or analyzed during this study are contained in this article.

Conflicts of Interest: The authors declare the following financial interests/personal relationships which may be considered as potential competing interests: Florinel Sava, Alin Velea, Angel Theodor Buruiana, Claudia Mihai, Elena Matei, and Teddy Tite have patent application to the State Office for Inventions and Trademarks—Romania.

References

1. Wang, Q.H.; Kalantar-Zadeh, K.; Kis, A.; Coleman, J.N.; Strano, M.S. Electronics and optoelectronics of two-dimensional transition metal dichalcogenides. *Nat. Nanotechnol.* **2012**, *7*, 699–712. [CrossRef] [PubMed]
2. Zhou, J.; Lin, J.; Huang, X.; Zhou, Y.; Chen, Y.; Xia, J.; Wang, H.; Xie, Y.; Yu, H.; Lei, J.; et al. A library of atomically thin metal chalcogenides. *Nature* **2018**, *556*, 355–359. [CrossRef] [PubMed]
3. Wilson, J.A.; Yoffe, A.D. The transition metal dichalcogenides discussion and interpretation of the observed optical, electrical and structural properties. *Adv. Phys.* **1969**, *18*, 193–335. [CrossRef]
4. Novoselov, K.S.; Geim, A.K.; Morozov, S.V.; Jiang, D.; Zhang, Y.; Dubonos, S.V.; Grigorieva, I.V.; Firsov, A.A. Electric field effect in atomically thin carbon films. *Science* **2004**, *306*, 666–669. [CrossRef] [PubMed]
5. Chen, S.; Ji, H.; Chou, H.; Li, Q.; Li, H.; Suk, J.W.; Piner, R.; Liao, L.; Cai, W.; Ruoff, R.S. Millimeter-Size Single-Crystal Graphene by Suppressing Evaporative Loss of Cu During Low Pressure Chemical Vapor Deposition. *Adv. Mater.* **2013**, *25*, 2062–2065. [CrossRef] [PubMed]
6. Zhou, S.; Gan, L.; Wang, D.; Li, H.; Zhai, T. Space-confined vapor deposition synthesis of two dimensional materials. *Nano Res.* **2018**, *11*, 2909–2931. [CrossRef]
7. O'Brien, M.; McEvoy, N.; Hallam, T.; Kim, H.-Y.; Berner, N.C.; Hanlon, D.; Lee, K.; Coleman, J.N.; Duesberg, G.S. Transition Metal Dichalcogenide Growth via Close Proximity Precursor Supply. *Sci. Rep.* **2014**, *4*, 7374. [CrossRef] [PubMed]
8. O'Brien, M.; McEvoy, N.; Hanlon, D.; Hallam, T.; Coleman, J.N.; Duesberg, G.S. Mapping of Low-Frequency Raman Modes in CVD-Grown Transition Metal Dichalcogenides: Layer Number, Stacking Orientation and Resonant Effects. *Sci. Rep.* **2016**, *6*, 19476. [CrossRef] [PubMed]
9. Suzuki, H.; Hashimoto, R.; Misawa, M.; Liu, Y.; Kishibuchi, M.; Ishimura, K.; Tsuruta, K.; Miyata, Y.; Hayashi, Y. Surface diffusion-limited growth of large and high-quality monolayer transition metal dichalcogenides in confined space of microreactor. *ACS Nano* **2022**, *16*, 11360–11373. [CrossRef]
10. Cong, C.; Shang, J.; Wu, X.; Cao, B.; Peimyoo, N.; Qiu, C.; Sun, L.; Yu, T. Synthesis and Optical Properties of Large-Area Single-Crystalline 2D Semiconductor WS_2 Monolayer from Chemical Vapor Deposition. *Adv. Opt. Mater.* **2014**, *2*, 131–136. [CrossRef]
11. Kang, K.; Godin, K.; Kim, Y.D.; Fu, S.; Cha, W.; Hone, J.; Yang, E.-H. Graphene-Assisted Antioxidation of Tungsten Disulfide Monolayers: Substrate and Electric-Field Effect. *Adv. Mater.* **2017**, *29*, 1603898. [CrossRef] [PubMed]
12. Wang, X.; Kang, K.; Chen, S.; Du, R.; Yang, E.-H. Location-specific growth and transfer of arrayed MoS_2 monolayers with controllable size. *2D Mater.* **2017**, *4*, 025093. [CrossRef]
13. Fu, S.; Kang, K.; Shayan, K.; Yoshimura, A.; Dadras, S.; Wang, X.; Zhang, L.; Chen, S.; Liu, N.; Jindal, A.; et al. Enabling room temperature ferromagnetism in monolayer MoS_2 via in situ iron-doping. *Nat. Commun.* **2020**, *11*, 2034. [CrossRef] [PubMed]
14. Zhang, X.; Nan, H.; Xiao, S.; Wan, X.; Ni, Z.; Gu, X.; Ostrikov, K. Shape-Uniform, High-Quality Monolayered MoS_2 Crystals for Gate-Tunable Photoluminescence. *ACS Appl. Mater. Interfaces* **2017**, *9*, 42121–42130. [CrossRef] [PubMed]
15. Mohapatra, P.K.; Deb, S.; Singh, B.P.; Vasa, P.; Dhar, S. Strictly monolayer large continuous MoS_2 films on diverse substrates and their luminescence properties. *Appl. Phys. Lett.* **2016**, *108*, 042101. [CrossRef]
16. Zhang, X.; Xiao, S.; Shi, L.; Nan, H.; Wan, X.; Gu, X.; Ni, Z.; Ostrikov, K. Large-size $Mo_{1-x}W_xS_2$ and $W_{1-x}Mo_xS_2$ (x = 0–0.5) monolayers by confined-space chemical vapor deposition. *Appl. Surf. Sci.* **2018**, *457*, 591–597. [CrossRef]
17. Mahjouri-Samani, M.; Tian, M.; Wang, K.; Boulesbaa, A.M.; Rouleau, C.; Puretzky, A.A.; McGuire, M.A.; Srijanto, B.R.; Xiao, K.; Eres, G.; et al. Digital Transfer Growth of Patterned 2D Metal Chalcogenides by Confined Nanoparticle Evaporation. *ACS Nano* **2014**, *8*, 11567–11575. [CrossRef] [PubMed]
18. Kim, K.S.; Lee, D.; Chang, C.S.; Seo, S.; Hu, Y.; Cha, S.; Kim, H.; Shin, J.; Lee, J.-H.; Lee, S.; et al. Non-epitaxial single-crystal 2D material growth by geometric confinement. *Nature* **2023**, *614*, 88–94. [CrossRef] [PubMed]

19. Stoica, T.; Stoica, M.; Duchamp, M.; Tiedemann, A.; Mantl, S.; Grützmacher, D.; Buca, D.; Kardynał, B.E. Vapor transport growth of MoS_2 nucleated on SiO_2 patterns and graphene flakes. *Nano Res.* **2016**, *9*, 3504–3514. [CrossRef]
20. Feng, Q.; Zhu, Y.; Hong, J.; Zhang, M.; Duan, W.; Mao, N.; Wu, J.; Xu, H.; Dong, F.; Lin, F.; et al. Growth of Large-Area 2D $MoS_{2(1-x)}Se_{2x}$ Semiconductor Alloys. *Adv. Mater.* **2014**, *26*, 2648–2653. [CrossRef]
21. Wu, S.; Huang, C.; Aivazian, G.; Ross, J.S.; Cobden, D.H.; Xu, X. Vapor-Solid Growth of High Optical Quality MoS_2 Monolayers with Near-Unity Valley Polarization. *ACS Nano* **2013**, *7*, 2768–2772. [CrossRef] [PubMed]
22. Catalán-Gómez, S.; Garg, S.; Redondo-Cubero, A.; Gordillo, N.; de Andrés, A.; Nucciarelli, F.; Kim, S.; Kung, P.; Pau, J.L. Photoluminescence enhancement of monolayer MoS_2 using plasmonic gallium nanoparticles. *Nanoscale Adv.* **2019**, *1*, 884–893. [CrossRef] [PubMed]
23. Chow, P.K.; Singh, E.; Viana, B.C.; Gao, J.; Luo, J.; Li, J.; Lin, Z.; Elías, A.L.; Shi, Y.; Wang, Z.; et al. Wetting of mono and few-layered WS_2 and MoS_2 films supported on Si/SiO_2 substrates. *ACS Nano* **2015**, *9*, 3023–3031. [CrossRef] [PubMed]
24. Venkata Subbaiah, Y.P.; Saji, K.J.; Tiwari, A. Atomically Thin MoS_2: A Versatile Nongraphene 2D Material. *Adv. Funct. Mater.* **2016**, *26*, 2046–2069. [CrossRef]
25. Trainer, D.J.; Nieminen, J.; Bobba, F.; Wang, B.; Xi, X.; Bansil, A.; Iavarone, M. Visualization of defect induced in-gap states in monolayer MoS_2. *NPJ 2D Mater. Appl.* **2022**, *6*, 13. [CrossRef]
26. Hong, J.; Hu, Z.; Probert, M.; Li, K.; Lv, D.; Yang, X.; Gu, L.; Mao, N.; Feng, Q.; Xie, L.; et al. Exploring atomic defects in molybdenum disulphide monolayers. *Nat. Commun.* **2015**, *6*, 6293. [CrossRef]
27. Li, H.; Zhang, Q.; Yap, C.C.R.; Tay, B.K.; Edwin, T.H.T.; Olivier, A.; Baillargeat, D. From Bulk to Monolayer MoS_2: Evolution of Raman Scattering. *Adv. Funct. Mater.* **2012**, *22*, 1385–1390. [CrossRef]
28. Liang, F.; Xu, H.; Wu, X.; Wang, C.; Luo, C.; Zhan, J. Raman spectroscopy characterization of two-dimensional materials. *Chin. Phys. B* **2018**, *27*, 037802. [CrossRef]
29. Frey, G.L.; Tenne, R.; Matthews, M.J.; Dresselhaus, M.S.; Dresselhaus, G. Raman and resonance Raman investigation of MoS_2 nanoparticles. *Phys. Rev. B* **1999**, *60*, 2883. [CrossRef]
30. Cortijo-Campos, S.; Prieto, C.; De Andrés, A. Size Effects in Single- and Few-Layer MoS_2 Nanoflakes: Impact on Raman Phonons and Photoluminescence. *Nanomaterials* **2022**, *12*, 1330. [CrossRef]
31. Gusakova, J.; Wang, X.; Shiau, L.L.; Krivosheeva, A.; Shaposhnikov, V.; Borisenko, V.; Gusakov, V.; Tay, B.K. Electronic properties of bulk and monolayer TMDs: Theoretical study within DFT framework (GVJ-2e method). *Phys. Status Solidi A* **2017**, *12*, 1700218. [CrossRef]
32. Roldan, R.; Silva-Guillen, J.A.; Lopez-Sancho, M.P.; Guinea, F.; Cappelluti, E.; Ordejon, P. Electronic properties of single-layer and multilayer transition metal dichalcogenides MX_2 (M = Mo, W and X = S, Se). *Ann. Phys.* **2014**, *526*, 347–357. [CrossRef]
33. Splendiani, A.; Sun, L.; Zhang, Y.; Li, T.; Kim, J.; Chim, C.-Y.; Galli, G.; Wang, F. Emerging Photoluminescence in Monolayer MoS_2. *Nano Lett.* **2010**, *10*, 1271–1275. [CrossRef] [PubMed]
34. Stacy, A.M.; Hodul, D.T. Raman spectra of IVb and VIb transition metal disulfides using laser energies near the absorption edges. *Phys. Chem. Solids* **1985**, *46*, 405–409. [CrossRef]
35. Xia, M.; Li, B.; Yin, K.; Capellini, G.; Niu, G.; Gong, Y.; Zhou, W.; Ajayan, P.M.; Xie, Y.-H. Spectroscopic Signatures of AA′ and AB Stacking of Chemical Vapor Deposited Bilayer MoS_2. *ACS Nano* **2015**, *9*, 12246–12254. [CrossRef] [PubMed]
36. Livneh, T.; Spanier, J.E. A comprehensive multiphonon spectral analysis in MoS_2. *2D Mater.* **2015**, *2*, 035003. [CrossRef]
37. Carvalho, B.R.; Wang, Y.; Mignuzzi, S.; Roy, D.; Terrones, M.; Fantini, C.; Crespi, V.H.; Malard, L.M.; Pimenta, M.A. Intervalley scattering by acoustic phonons in two-dimensional MoS_2 revealed by double-resonance Raman spectroscopy. *Nat. Commun.* **2017**, *8*, 14670. [CrossRef]
38. Pimenta, M.A.; del Corro, E.; Carvalho, B.R.; Fantini, C.; Malard, L.M. Comparative Study of Raman Spectroscopy in Graphene and MoS_2-type Transition Metal Dichalcogenides. *Acc. Chem. Res.* **2015**, *48*, 41–47. [CrossRef]
39. Mignuzzi, S.; Pollard, A.J.; Bonini, N.; Brennan, B.; Gilmore, I.S.; Pimenta, M.A.; Richards, D.; Roy, D. Effect of disorder on Raman scattering of single-layer MoS_2. *Phys. Rev. B* **2015**, *91*, 195411. [CrossRef]
40. Popescu, M.; Sava, F.; Lőrinczi, A.; Velea, A. Disorder in order: Silicon versus graphene. *Phys. Status Solidi B* **2013**, *250*, 1008–1010. [CrossRef]
41. Popescu, M.; Sava, F.; Lőrinczi, A.; Velea, A.; Simandan, I.D. Nanocarbon embedded chalcogenides. Onion-like model. *J. Optoelectron. Adv. Mater.* **2011**, *13*, 1450–1453.
42. Jung, Y.; Shen, J.; Liu, Y.; Woods, J.M.; Sun, Y.; Cha, J.J. Metal seed layer thickness-induced transition from vertical to horizontal growth of MoS_2 and WS_2. *Nano Lett.* **2014**, *14*, 6842–6849. [CrossRef] [PubMed]
43. Wei, B.; Li, Y.; Yun, T.; Li, Y.; Gui, T.; Yu, W.; Mu, H.; Cui, N.; Chen, W.; Lin, S. Triply degenerate semimetal $PtBi_2$ as van der Waals contact interlayer in two-dimensional transistor. *Mater. Futures* **2024**, *3*, 025302. [CrossRef]
44. Gong, Y.; Xu, Z.-Q.; Li, D.; Zhang, J.; Aharonovich, I.; Zhang, Y. Two-Dimensional Hexagonal Boron Nitride for Building Next-Generation Energy-Efficient Devices. *ACS Energy Lett.* **2021**, *6*, 985–996. [CrossRef]
45. Deng, D.; Novoselov, K.; Fu, Q.; Zheng, N.; Tian, Z.; Bao, X. Catalysis with two-dimensional materials and their heterostructures. *Nat. Nanotech* **2016**, *11*, 218–230. [CrossRef] [PubMed]
46. Ye, G.; Gong, Y.; Lin, J.; Li, B.; He, Y.; Pantelides, S.T.; Zhou, W.; Vajtai, R.; Ajayan, P.M. Defects engineered monolayer MoS_2 for improved hydrogen evolution reaction. *Nano Lett.* **2016**, *16*, 1097–1103. [CrossRef]

47. Anbalagan, A.k.; Hu, F.-C.; Chan, W.K.; Gandhi, A.C.; Gupta, S.; Chaudhary, M.; Chuang, K.-W.; Ramesh, A.K.; Billo, T.; Sabbah, A.; et al. Gamma-Ray Irradiation Induced Ultrahigh Room-Temperature Ferromagnetism in MoS_2 Sputtered Few-Layered Thin Films. *ACS Nano* **2023**, *17*, 6555–6564. [CrossRef] [PubMed]
48. Kumar, R.R.; Habib, M.R.; Khan, A.; Chen, P.-C.; Murugesan, T.; Gupta, S.; Anbalagan, A.k.; Tai, N.-H.; Lee, C.-H.; Lin, H.-N. Sulfur Monovacancies in Liquid-Exfoliated MoS_2 Nanosheets for NO_2 Gas Sensing. *ACS Appl. Nano Mater.* **2021**, *4*, 9459–9470. [CrossRef]
49. Kumara, P.; Viswanath, B. Horizontally and vertically aligned growth of strained MoS_2 layers with dissimilar wetting and catalytic behaviors. *CrystEngComm* **2017**, *19*, 5068–5078. [CrossRef]
50. Liu, X.; Jiang, X.; Shao, G.; Xiang, H.; Li, Z.; Jin, Y.; Chen, Y.; Jiang, H.; Li, H.; Shui, J.; et al. Activating the Electrocatalysis of MoS_2 Basal Plane for Hydrogen Evolution via Atomic Defect Configurations. *Small* **2022**, *18*, 2200601. [CrossRef]
51. Bruix, A.; Füchtbauer, H.G.; Tuxen, A.K.; Walton, A.S.; Andersen, M.; Porsgaard, S.; Besenbacher, F.; Hammer, B.; Lauritsen, J.V. In Situ Detection of Active Edge Sites in Single-Layer MoS_2 Catalysts. *ACS Nano* **2015**, *9*, 9322–9330. [CrossRef] [PubMed]
52. Yang, L.; Zhang, J.; Feng, C.; Xu, G.; Xie, C.; Yuan, X.; Xiang, B. MoS_2 nanosheet/MoS_2 flake homostructures for efficient electrocatalytic hydrogen evolution. *Mater. Res. Express* **2019**, *6*, 085005. [CrossRef]
53. Attanayake, N.H.; Thenuwara, A.C.; Patra, A.; Aulin, Y.V.; Tran, T.M.; Chakraborty, H.; Borguet, E.; Klein, M.L.; Perdew, J.P.; Strongin, D.R. Effect of Intercalated Metals on the Electrocatalytic Activity of 1T-MoS_2 for the Hydrogen Evolution Reaction. *ACS Energy Lett.* **2018**, *3*, 7–13. [CrossRef]